

NEAR- TO MID-INFRARED OBSERVATIONS OF GALAXY MERGERS: NGC2782 AND NGC7727

TAKASHI ONAKA, TOMOHIKO NAKAMURA¹, ITSUKI SAKON, AND RONIN WU²

Department of Astronomy, Graduate School of Science, The University of Tokyo, Bunkyo-ku, Tokyo 113-0033, Japan

RYOU OHSAWA

Institute of Astronomy, Graduate School of Science, The University of Tokyo, Mitaka Tokyo 181-0015, Japan

HIDEHIRO KANEDA

Graduate School of Science, Nagoya University, Chikusa-ku, Nagoya 464-8602, Japan

VIANNEY LEBOUTEILLER

Laboratoire AIM - CEA Saclay, Bat. 709, Piece 267, Orme des Merisiers, 91191 Gif-sur-Yvette, France

THOMAS L. ROELLIG

NASA Ames Research Center, MS 245-6, Moffett Field, California 94035-1000, U.S.A.

¹Present address: Recruit Communications Co. Ltd, Tokyo, Japan

²Present address: LERMA, Observatoire de Paris, PSL Research University, CNRS, Sorbonne Université, UPMC Paris 06, 92190, Meudon, France

ABSTRACT

We present the results of near- to mid-infrared (NIR to MIR) imaging and NIR spectroscopic observations of two galaxy mergers, NGC 2782 (Arp 215) and NGC 7727 (Arp 222), with the Infrared Camera on board *AKARI*. NGC 2782 shows extended MIR emission in the eastern side of the galaxy, which corresponds to the eastern tidal tail seen in the H I 21 cm map, while NGC 7727 shows extended MIR emission in the north of the galaxy, which is similar to the plumes seen in the residual image at the *K*-band after subtracting a galaxy model. Both extended structures are thought to have formed associated with their merger events. They show excess emission at 7–15 μm , which can be attributed to emission from polycyclic aromatic hydrocarbons (PAHs), while the observed spectral energy distributions decline longward of 24 μm , suggesting that very small grains (VSGs) are deficient. These characteristics of the observed MIR spectral energy distribution may be explained if PAHs are formed by fragmentation of VSGs during merger events. The star formation rate is estimated from the MIR PAH emission in the eastern tail region of NGC 2782 and it is in fair agreement with those estimated from H α and [C II] 158 μm . MIR observations are efficient for the study of dust processing and structures formed during merger events.

Keywords: infrared: galaxies – galaxies: ISM — galaxies: interactions – galaxies: star formation – galaxies individual (NGC2782, NGC7727)

1. INTRODUCTION

Dust grains retain most of the heavy elements and play significant roles in the thermal balance and chemistry

in the interstellar medium (ISM). Thermal emission in the far-infrared (FIR) from submicron- size dust is often used as a useful measure for the star-formation rate (SFR) for the optically thick case (Kennicutt 1998), while the SFR is also known to correlate well with the strengths of the emission features in the mid-infrared

(MIR, e.g., Peeters et al. 2004; Pope et al. 2008; Shipley et al. 2016), whose major bands appear at 3.3, 6.2, 7.7, 8.6, 11.3, and 16.4 μm . They are thought to originate from very small carbonaceous dust that contains polycyclic aromatic hydrocarbons (PAH, Tielens 2008) or PAH-like atomic groups, while alternative carriers, such as quenched carbonaceous composite (QCC, Sakata et al. 1984) or mixed aromatic-aliphatic organic nanoparticles (MAON, Kwok & Zhang 2011), have also been proposed. In the following, we call these emission features PAH features and the carriers PAHs.

The formation and destruction as well as lifecycle of dust grains in galaxies are vital for the understanding of star-formation and evolution of galaxies. The properties and the formation/destruction processes of carriers of the PAH features are of particular interest because they are so conspicuous in the MIR and the relative band ratios should be useful to study the physical conditions of the environment from which the emission features arise (Draine & Li 2001; Tielens 2008). While several theoretical studies have been carried out (e.g., Dwek & Scalo 1980; Jones & Nuth 2011), little is so far studied observationally about the lifecycle of dust grains in the ISM. It still remains unclear where the carriers of the PAH features are formed. They may be formed in carbon-rich stars (Galliano et al. 2008a; Paradis et al. 2008) or in dense clouds (Herbst 1991; Sandstrom et al. 2010). Recent observations with *AKARI* and *SOFIA* suggest that PAHs are also formed by fragmentation of large carbonaceous grains in shocks associated with a supernova, a galactic wind, or an outflow from a planetary nebula (Onaka et al. 2010a; Seok et al. 2012; Lau et al. 2016).

The PAH features have been detected not only in the disks of galaxies, but also in the halos of galaxies. Engelbracht et al. (2006) and Beirão et al. (2008) reported detection of the PAH emission in the halo of M82. Kaneda et al. (2010) suggested that PAHs have been expelled both by the superwind and the galaxy interaction from the disk of M82. Survival of PAHs in such harsh environments is another interesting issue for the study of lifecycle and destruction of PAHs (e.g., Micelotta et al. 2010). The PAH features in galaxy halos seem to have a lower 7.7 μm to 11.3 μm band ratio than that in galactic disks (Irwin & Madden 2006; Galliano et al. 2008b). A similar small ratio is also indicated in the interarm region (Sakon et al. 2007) as well as in a filamentary structure associated with the galactic wind (Onaka et al. 2010a). The small ratio may be attributed to processing of the band carriers in these tenuous regions or could be related to their formation process. Observations of the PAH features in extended structures in galaxies are thus important for the study of dust processing.

In this paper, we report the results of near-infrared (NIR) to MIR observations of two galaxy mergers, NGC

2782 (Arp 215) and NGC 7727 (Arp 222), with the Infrared Camera (IRC) on board *AKARI* (Onaka et al. 2007b) to study the properties of dust grains associated with extended structures produced by merger events and their possible processing in violent conditions.

NGC2787 is a spiral galaxy classified as Sa(s) Peculiar (Sandage & Tammann 1981) or as SABa(rs) Peculiar by de Vaucouleurs et al. (1991) at a distance of 39.5 Mpc (Knierman et al. 2013). It is a minor merger with an age of 200–300 Myr old (Smith 1994; Knierman et al. 2013). NGC 2782 shows long tidal tails extending both in the west and east directions in the H I map (Smith 1994). A tidal dwarf galaxy candidate (TDGC) was discovered in the eastern side of the galaxy (Yoshida et al. 1994). It harbors a starburst both in the central and circumnuclear regions (Jogee et al. 1999). Gas motion in the central part of the galaxy is studied in detail by interferometric CO observations (Hunt et al. 2008). NGC 2782 was originally classified as a Seyfert galaxy, but no direct sign of AGN had been obtained (Boer et al. 1992) until recent X-ray observations found clear evidence for the presence of a low-luminosity AGN (Tzanavaris & Georgantopoulos 2007; Bravo-Guerrero & Stevens 2017). Star-formation in the tidal tails was studied extensively based on observations of CO (J=1-0), H α , and [C II] 158 μm (Smith et al. 1999; Knierman et al. 2013).

NGC 7727 is also a merger at a distance of 25 Mpc and of an age of 1.3 Gyr old (Georgakakis et al. 2000). It is classified as Sa Peculiar by Sandage & Tammann (1981) and SAB(s)a Peculiar by de Vaucouleurs et al. (1991). The *K*-band image suggests plumes extending to the north of the galaxy from the nucleus (Rothberg & Joseph 2004). We present the results of IRC NIR to MIR imaging observations of the two galaxies as well as NIR spectroscopy of the central regions of both galaxies. Star-formation in interacting galaxies has been extensively studied in the IR (e.g., Smith et al. 2007b; Brassington et al. 2015). In this paper, we concentrate on the dust properties in extended structures in the two galaxies.

2. OBSERVATIONS AND DATA REDUCTION

The *AKARI*/IRC imaging observations of NGC 2782 and NGC 7727 were carried out as part of the mission program “ISM in our Galaxy and nearby galaxies” (ISMNG, Kaneda et al. 2009a) in the cryogenic mission phase. The observations were made with the two-filter modes of the IRC. 10' \times 10' images at bands N3 (3.2 μm), N4 (4.1 μm), S7 (7 μm), and S11 (11 μm) were obtained with the AOT IRC02 a;N in the same pointing observation, while images at bands L15 (15 μm) and L24 (24 μm) were obtained with AOT IRC02 a;L in a different pointing observation. Details of the operations

of both AOTs are given in [Onaka et al. \(2007b\)](#). NIR IRC spectroscopy of the two galaxies was carried out in the warm mission phase of *AKARI* with the grism mode (AOT: IRCZ4 b;Ns), which provided long slit

spectroscopy of a $5'' \times 40''$ area for $2.5\text{--}5.0\ \mu\text{m}$ with a spectral resolution of about $0.03\ \mu\text{m}$ ([Ohyama et al. 2007](#)). The performance of the IRC in the warm mission phase is given in [Onaka et al. \(2010b\)](#). A log of the present observations is summarized in [Table 1](#).

Table 1. IRC observation log

Source name	Mode	Pointing ID	AOT ^a	Observation date
NGC 2782	imaging (3.2, 4.1, 7, 11 μm)	1400452.1	IRC02 a;N	2006 October 31
	imaging (15, 24 μm)	1401038.1	IRC02 a;L	2007 April 29
	spectroscopy (2.5–5.0 μm)	1420364.1	IRCZ4	2009 April 28
	spectroscopy (2.5–5.0 μm)	1420364.2	IRCZ4	2009 April 28
NGC 7727	imaging (3.2, 4.1, 7, 11 μm)	1402685.1	IRC02 a;N	2007 June 11
	imaging (15, 24 μm)	1402686.1	IRC02 a;L	2007 June 11
	spectroscopy (2.5–5.0 μm)	1420386.1	IRCZ4	2008 December 11

^aSee [Onaka et al. \(2007b\)](#) and [Onaka et al. \(2009\)](#) for details of the AOTs in the cold and warm mission phases, respectively.

The imaging data were processed by the data reduction toolkit for the IRC imaging version 20110304. Then, we corrected for the effects of array anomalies in the NIR images (N3 and N4), such as muxbleed and column pulldown, by our own developed software, which subtracts fitted polynomial functions from the data of the affected rows and columns (cf., [Carey et al. 2004](#)). For the MIR images (S7, S11, L15, and L24), we applied the Richardson-Lucy method with noise suppression using the wavelet transform ([Richardson 1972](#); [Lucy 1974](#); [Starck & Murtagh 1994](#)) to reduce the noise and restore the images taking account of the point spread functions (PSFs) of each filter band. Then, the restored MIR images were convolved with a Gaussian to have the same FWHM of $7''$. Finally we took a median of the emission outside of the galaxy and associated extended structures as the sky background and subtracted it from the observed image. The uncertainty in the estimate of the sky background is included in the photometry error.

NIR spectroscopy was made toward the center of the galaxy. Due to the pointing accuracy of *AKARI*, the actual positions at which spectroscopic observations were made were slightly off the center (see § 3 and [Table 2](#)). The data were processed by the data reduction toolkit for the phase 3 (warm mission phase) IRC spectroscopy version 20160324, which included the latest wavelength calibration ([Baba et al. 2016](#)). The spectrum was extracted for the brightest part of an area of $5'' \times 8''.7$ (6 pixels in the slit direction) in the slit for each galaxy. The central positions of the spectra are listed in [Table 2](#)

and the spectrum-extracted areas are indicated by the white rectangles in [Figures 3 and 6](#). For NGC 2782, we have taken spectra with two pointing observations at slightly different positions ($\sim 1''$). The flux levels are slightly different, but the spectral shapes are almost the same. We scale the fainter spectrum (Pointing ID: 1420364.1) to the brighter one (Pointing ID: 1420364.2) and co-add them together to reduce the noise. The position in [Table 1](#) refers to the spectrum extracted from the data of 1420364.2. NGC 7727 was observed only once.

In addition to the IRC observations, we retrieved *Spitzer*/Infrared Spectrograph (IRS) data of NGC 2782 from the Combined Atlas of Sources with *Spitzer*/IRS Spectra (CASSIS; [Lebouteiller et al. 2011, 2015](#)). NGC 2782 (AORKEY: 3856986) was observed with the short-low (SL) and long-low (LL) modules that provided spectra between $5.2\text{--}37.2\ \mu\text{m}$ with a spectral resolving power of 64–128 ([Houck et al. 2004](#)). The spectral extraction was performed with Smart/AdOpt ([Higdon et al. 2004](#); [Lebouteiller et al. 2010](#)). The AdOpt tool enables the simultaneous extraction of blended sources in the IRS apertures. The sources are either point like or they can be described by the convolution of the PSF profile with an intrinsic source shape (e.g., 2D Gaussian). Only the spectrum of the central part of the galaxy has a sufficient signal-to-noise ratio and is extracted. The spatial profile of the extracted spectrum is broader than a point source and it can be well approximated by a compact and an extended component. We estimate that the

FWHMs of the compact and the extended components are $4''$ and $14''$, respectively, and extract the spectrum of each component in each module (SL and LL). The

center positions of each component are listed in Table 2. NGC 7727 has not been observed with the IRS.

Table 2. Positions of the spectrum extracted

Source	Instrument	R.A. (J2000)	Decl. (J2000)	Note
NGC 2782	IRC ^a	09 ^h 14 ^m 05 ^s .3	40°06′53″.4	Extracted for an area of $5'' \times 8''$.
NGC 2782c	IRS	09 ^h 14 ^m 05 ^s .3	40°06′49″.7	Compact component (FWHM = $4''$)
NGC 2782e	IRS	09 ^h 14 ^m 05 ^s .2	40°06′49″.3	Extended component (FWHM = $14''$)
NGC 7727	IRC	23 ^h 39 ^m 53 ^s .9	-12°17′30″.5	Extracted for an area of $5'' \times 8''$.

^aThe position of the brighter spectrum extracted (see text).

3. RESULTS

3.1. NGC 2782

NIR to MIR 6-band IRC images of the central part ($5' \times 5'$) of NGC 2782 are shown in Figures 1. The NIR images of N3 and N4 (Figures 1a and b) both clearly show extended emission in the eastern side of the galaxy, which is also seen in optical images (Smith 1994). In the MIR images (Figures 1c–f) it is invisible, suggesting that this extended structure consists only of stellar components without dust. In fact, no gas emission has been detected in this region. It is likely a stellar remnant of the minor galaxy that passed through the major galaxy with its interstellar materials being stripped off (Smith 1994).

The images at the bands S7, S11, and L15 show an arc-like bright emission structure in the western side of the galaxy (see also Figure 3), which is also seen as one of the ripples in optical images (Smith 1994; Jogee et al. 1999). In the N3 and N4 images, the emission of the stellar disk overlaps with the arc-like ripple structure, but it can still be recognized. It becomes faint in the L24 image. In addition to the ripple, the S7 and S11 images show extended emission in the eastern side of the galaxy. We call it the tail structure. The tail structure is not seen in the N3 and N4 images, suggesting that it is not associated with stellar emission, but comes from the ISM of the galaxy.

To show the tail structure more clearly, an artificial color image of N3 in blue and S7 in green was created as shown in Figure 2, on which the red contours of H I 21 cm intensity are superposed (Smith 1994). The H I 21 cm data show a very long tail in the western side, at which the IR emission is not detected, and a relatively compact tail in the eastern side, which delineates the tail structure seen at S7 (green color) nicely. Since both

H I tails must have been formed by the collision event, the tail structure seen at S7 and S11 is suggested to have also been formed together with the eastern H I tail during the collision event. In the further east, the stellar remnant is clearly seen only at N3 (blue color). The white color of the center and ripple regions suggests that they are bright both at N3 and S7.

Figure 3 shows an enlarged S7 image to indicate these structures clearly. The blue dashed rectangles in the tail structure indicate the locations of massive H I clouds as well as the TDGC (Smith 1994; Knierman et al. 2013). The emission at S7 shows good correlation with the regions of the massive H I clouds. There may be an enhancement in S7 even at the position of the TDGC. Figure 3 also suggests that the emission at S7 becomes strong along the optical dust lanes (Jogee et al. 1999) that are indicated by the black straight dashed lines.

Figure 4 shows the NIR and MIR spectra of the central part of NGC 2782. Note that units of the spectra are different; the NIR spectrum (Figure 4a) is in units of MJy sr⁻¹, while the spectra in Figures 4b and c are in units of Jy, for which the source sizes are assumed as described in §2. The NIR spectrum (Figure 4a) is extracted from the white rectangle in Figure 3 and the MIR spectra are taken nearly at the center of the galaxy (Table 2). The observed positions of each spectrum are not exactly the same and thus the relative comparison of the spectra needs caution. The NIR spectrum clearly shows the presence of the PAH $3.3 \mu\text{m}$ band as well as the emission from aliphatic C-H bonds at $3.4 \mu\text{m}$. The emission of H I Br α at $4.05 \mu\text{m}$ is barely seen, but no other gas emission features are detected. In the IRS SL spectra, the PAH features at 6.2 , 7.7 , 8.6 , and $11.3 \mu\text{m}$ are clearly seen in both compact and extended components (Figure 4b). The [Ne II] $12.8 \mu\text{m}$ overlaps with the PAH $12.7 \mu\text{m}$ feature. The compact component is

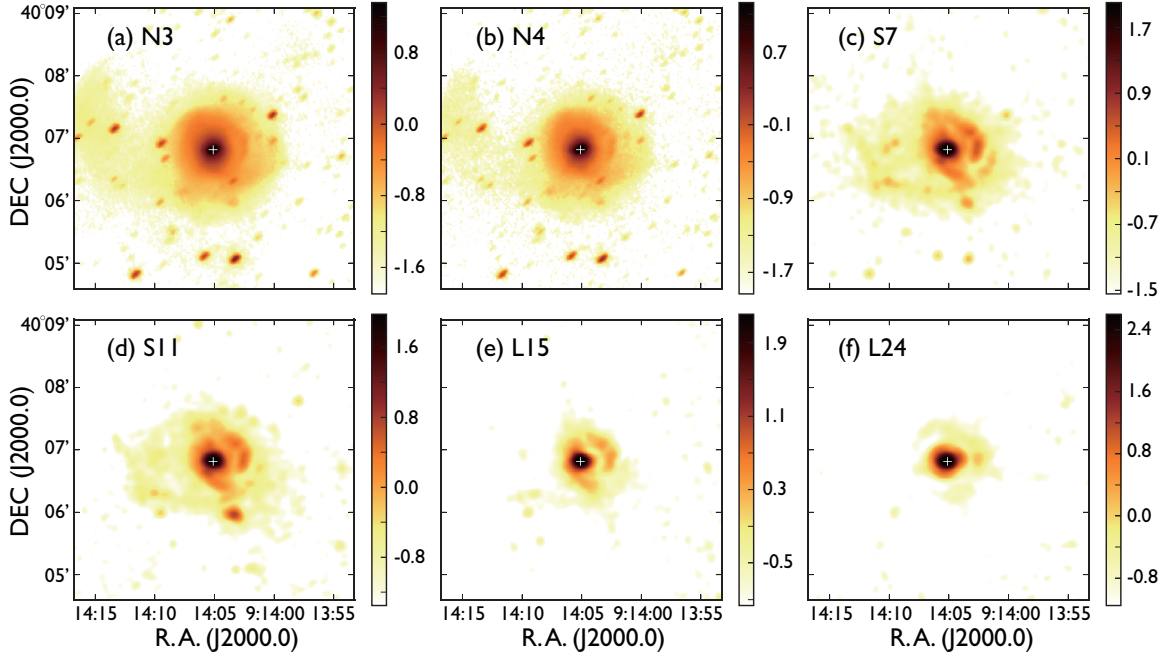


Figure 1. IRC images of NGC2782 at the bands (a) N3 ($3.2\ \mu\text{m}$), (b) N4 ($4.1\ \mu\text{m}$), (c) S7 ($7\ \mu\text{m}$), (d) S11 ($11\ \mu\text{m}$), (e) L15 ($15\ \mu\text{m}$), and (f) L24 ($24\ \mu\text{m}$). The center of the galaxy (RA, DEC) = ($09^{\text{h}}15^{\text{m}}05^{\text{s}}.1$, $40^{\circ}06'49''.0$) (J2000.0) is indicated by the white cross in each image. The color bar scale is in units of $\log(\text{MJy sr}^{-1})$.

slightly brighter than the extended component up to around $12\ \mu\text{m}$, above which the flux of the compact component sharply increases. In the IRS LL spectra, the PAH $17\ \mu\text{m}$ complex, [Ne III] $15.6\ \mu\text{m}$, [S III] 18.7 and $33.5\ \mu\text{m}$, and [Si II] $34.8\ \mu\text{m}$ are seen in both components. The compact component is relatively brighter in the ionized gas lines, while the extended component has relatively brighter [Si II], suggesting the dominance of emission from photo-dissociation regions (PDRs). There seems to be no clear sign for the presence of an AGN, such as strong [Ne V] $14.3\ \mu\text{m}$ or [O IV] $26\ \mu\text{m}$ emission, in both spectra (Armus et al. 2007; Farrah et al. 2007). Upper limits of both line intensities relative to the [Ne II] $12.8\ \mu\text{m}$ intensity are estimated as about 20%, which suggests that the AGN contribution to the MIR emission is less than 10% (Petric et al. 2011). The presence of an AGN is not confirmed by the present spectroscopy.

3.2. NGC7727

Figure 5 shows 6-band IRC images of the central part ($5' \times 5'$) of NGC7727. Compared to NGC 2782, the flux is concentrated on the galaxy center. In the S7 image, plume-like structures appear in the northern side of the galaxy (see also Figure 6), which becomes clearer in the S11 image. In the L15 image, the structures become fainter, but their trace is still visible. They almost fade away at L24. In the N3 and N4 images, part of the plumes are barely seen as emission extending to the north-east. Figure 6 shows an enlarged S7 image to indi-

cate these structures clearly as well as the region where the IRC NIR spectrum is extracted. Similar, but more diffuse plume structures are seen in the residual image in *K*-band after subtracting a galaxy model (Rothberg & Joseph 2004). The structures are named plume 1 and plume 2 as shown in the figure. We note that the intensity distribution around the center is slightly shifted toward east from the center position of the galaxy indicated by the white cross. We estimate the intensity of the central part of the galaxy within the yellow circle (see §4).

Figure 7 shows the *AKARI*/IRC NIR spectrum of the central region of NGC 7727. There seem to be no clear emission nor absorption features in the spectrum. A shallow, broad dent at around $4.5\ \mu\text{m}$ may be attributed to the CO fundamental vibration absorption, but the present data do not have a sufficient quality to confirm it. Compared to the NIR spectrum of NGC 2782 (Figure 4a), the NIR continuum of NGC 7727 is bluer, suggesting the dominance of the contribution from the stellar continuum over the emission from the ISM. The absence of H I recombination lines and the PAH features suggests low star-formation activities in the central region of NGC 7727.

4. DISCUSSION

4.1. NGC 2782

The MIR images at S7 and S11 show a tail structure in the eastern side of the galaxy, which has a good correspondence with the structure of the eastern H I tidal tail.

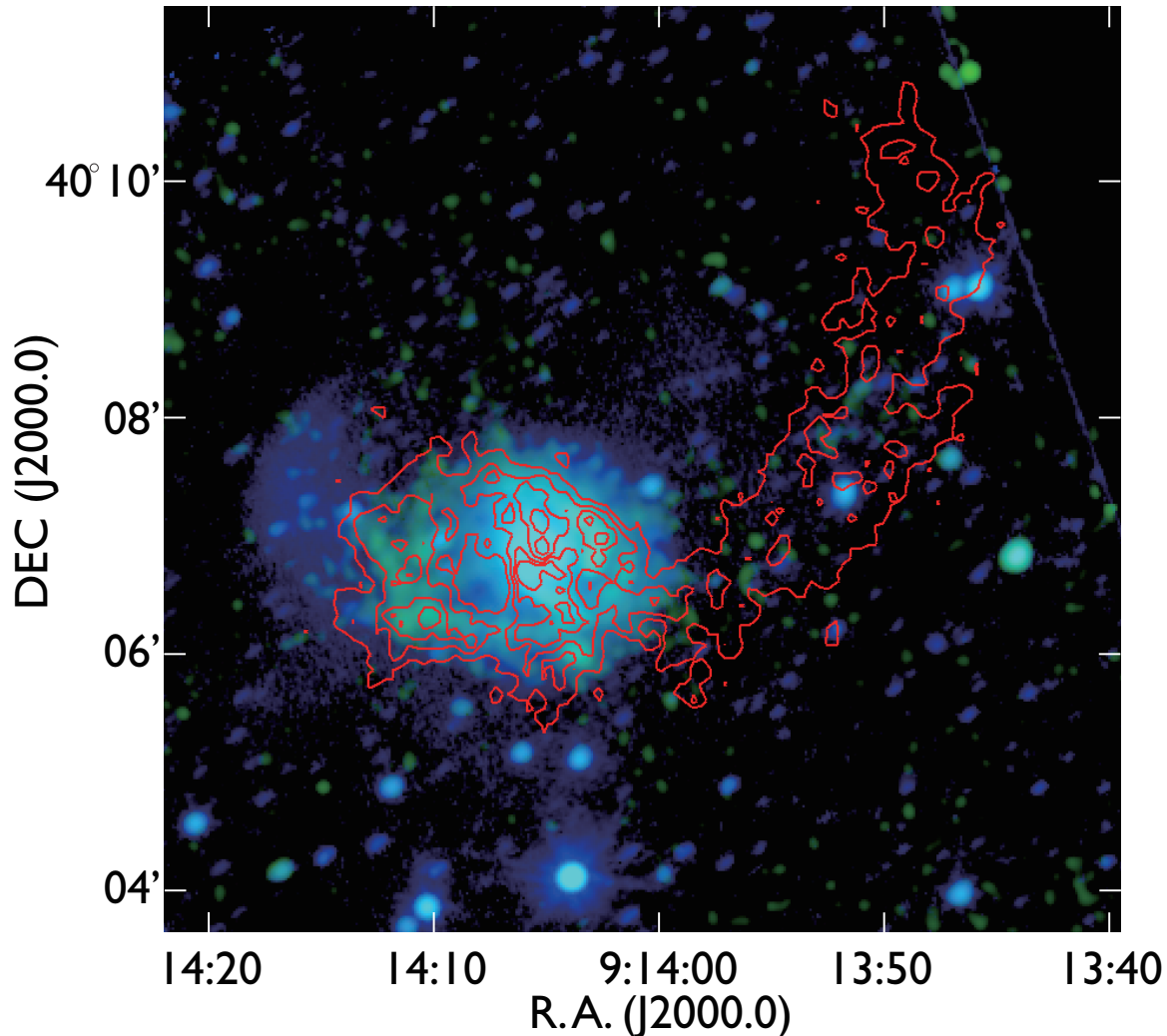


Figure 2. Artificial color image of NGC 2782. Blue and green colors correspond to N3 ($3.2 \mu\text{m}$) and S7 ($7 \mu\text{m}$) intensities, respectively. The superposed contours in red are the VLA H I 21 cm line intensities (Smith 1994) taken from the NASA/IPAC Extragalactic Database (NED).

In Figure 4, the spectral range that each filter of the IRC covers is indicated by the arrows. The emission of the PAH 6.2 and $7.7 \mu\text{m}$ bands dominates band S7 (Ishihara et al. 2007). In the S11 image, the 11.3 and $12.7 \mu\text{m}$ PAH bands are dominant features together with [Ne II] $12.8 \mu\text{m}$. Although there is no spectroscopic information for this observation with *AKARI*, we assume that the S7 and S11 images trace the PAH emission also for regions other than the center (cf., Onaka et al. 2010a). On the other hand, the L15 and L24 do not contain strong dust band features and they trace mostly the continuum emission.

Figure 8 shows the band ratio maps of NGC 2782. The intensity ratios of the 6.2 and $7.7 \mu\text{m}$ to the $11.3 \mu\text{m}$ bands are supposed to be sensitive to the ionization fraction and the size distribution of PAHs (Draine & Li 2001; Tielens 2008). The ratio of S7 to S11 can be regarded as a proxy for this band ratio. Figure 8a shows that

it is almost constant over the entire galaxy, including the central and extended regions, at around the values of ~ 1.2 . The figure does not indicate any systematic trend with the extended structures. The constant ratio suggests that the properties of PAHs, in particular their ionization fraction, do not vary appreciably in the galaxy.

The L24 to S11 color map shows that the ratio is high at the central part of the galaxy. This trend is also seen in the spectrum (Figure 4c). The ripple region may have slightly larger ratios (~ 1.8), but the region with larger ratios does not show good spatial correlation with the structure seen in the S7 image (Figure 3). The ratio is relatively low at the eastern tail. In general, the ratio of the $25 \mu\text{m}$ to $12 \mu\text{m}$ increases with the incident radiation field and thus with the star-formation activity (Dale et al. 2001; Sakon et al. 2006; Onaka et al. 2007a). Alternatively, the MIR continuum emission also increases with

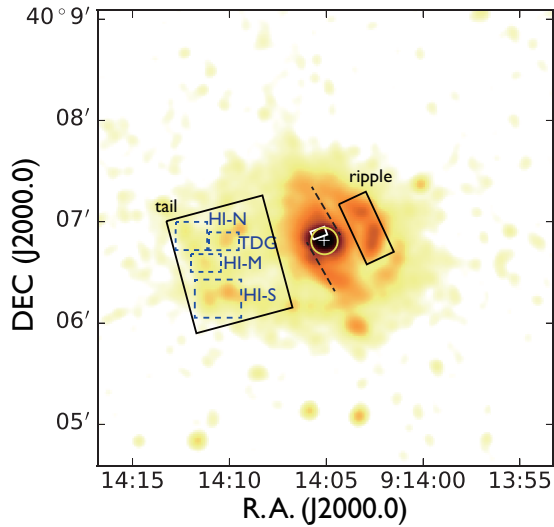


Figure 3. Enlarged S7 image of NGC 2782. The white cross symbol indicates the center position of the galaxy ($09^{\text{h}}14^{\text{m}}05^{\text{s}}.1$, $40^{\circ}06'49''.0$) and the yellow circle shows the central $8''$ region of the galaxy where the center flux is extracted (see § 4). The black solid rectangles indicate the areas where the fluxes are extracted for the ripple ($40'' \times 18''$) and the tail ($70'' \times 60''$) regions (see § 4.1). The blue dashed rectangular regions indicate the locations of massive H I clouds and the TDGC (Knierman et al. 2013). The black straight dashed lines show the locations of the dust lanes seen in optical images (Jogee et al. 1999). The white rectangle near the center indicates the area where the IRC NIR spectrum (Figure 4a) is extracted.

the presence of an AGN (Armus et al. 2007; Tommasin et al. 2010). Since no clear sign of AGN is recognized in the spectrum, the large L24 to S11 ratio comes more likely from the enhanced star-formation in the central part of the galaxy as suggested by previous investigations (Bravo-Guerrero & Stevens 2017, and references therein).

Ripples are thought to be formed during galaxy collisions and several mechanisms have been proposed for the ripple formation in mergers. Smith (1994) gives a summary of the mechanisms in detail, which includes radial oscillations in the stars and gas due to the head-on collision (Wallin & Stuck-Marcell 1988), ripples from the debris of the smaller mass galaxy (Quinn 1984; Henquist & Quinn 1988), tidal structures falling back into the remnant (Hernquist & Spergel 1992), stripped matter from a companion disk galaxy (Henquist & Quinn 1988), a distorted spiral density wave pattern perturbed by an encounter with another galaxy (Thomson & Wright 1990; Howard et al. 1993), and star formation triggered by shocks due to galactic winds (Fabian et al. 1980). The present result does not show evidence for an increase in the star-formation in the ripple.

To investigate the spectral energy distribution (SED) of each region in NGC 2782 more in detail, we made photometry at the center, ripple, and tail regions en-

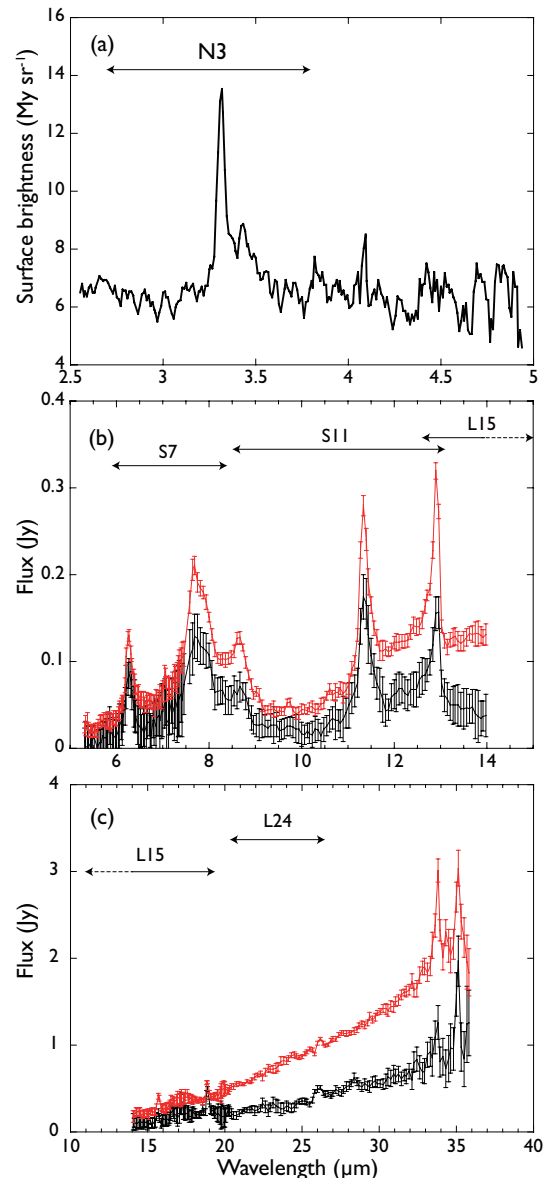


Figure 4. Infrared spectra of the center region of NGC 2782. (a) *AKARI*/IRC NIR spectrum extracted from the area indicated by the white rectangle in Figure 3. (b) *Spitzer*/IRS SL spectrum and (c) LL spectrum. The IRS spectra are extracted at the center of the galaxy (Table 2), assuming the source sizes as described in the text. In (b) and (c), the central compact component is indicated by the red lines and the extended component by the black lines. The arrows in the top of each figure indicate the e-folding response range of the IRC filters (Onaka et al. 2007b). The response of L15 filter spans the SL and LL spectral ranges.

closed by the circle and the solid rectangles in Figure 3. The data of N3 are used as a reference point to estimate the contribution from the stellar component. The spectrum of the stellar component is simply assumed to be given by the average stellar spectrum of the fluxes of red giant stars used in the flux calibration as in Onaka et al. (2010a). The assumed stellar contribution is less than 10% except for the N4 data, in which it amounts

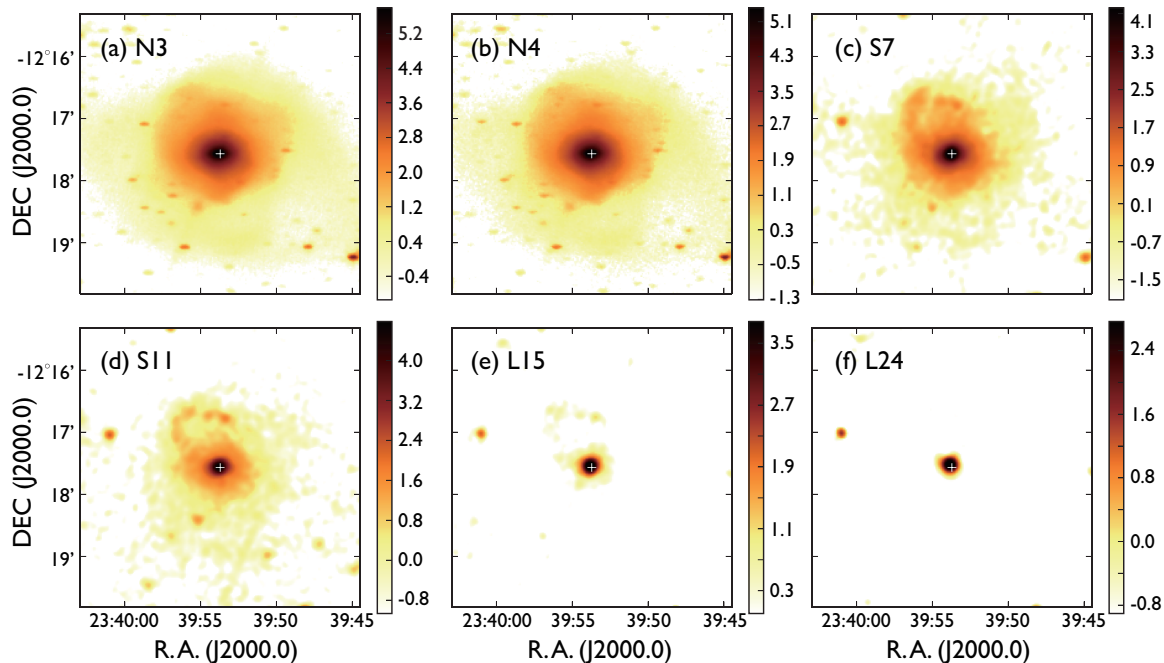


Figure 5. IRC images of NGC 7727 at the bands (a) N3 ($3.2 \mu\text{m}$), (b) N4 ($4.1 \mu\text{m}$), (c) S7 ($7 \mu\text{m}$), (d) S11 ($11 \mu\text{m}$), (e) L15 ($15 \mu\text{m}$), and (f) L24 ($24 \mu\text{m}$). The center of the galaxy (RA, DEC) = ($23^{\text{h}}39^{\text{m}}53^{\text{s}}.7$, $-12^{\circ}17'34''.0$) (J2000.0) is indicated by the white cross in each image. The color bar scale is in units of $\log(\text{MJy sr}^{-1})$.

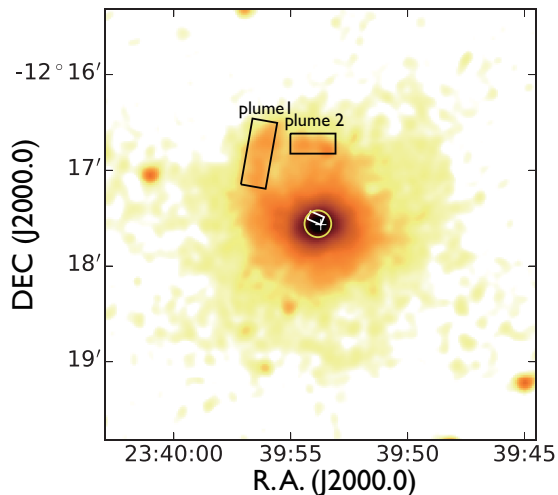


Figure 6. Enlarged S7 image of NGC 7727. The white cross indicates the center position of the galaxy ($23^{\text{h}}39^{\text{m}}53^{\text{s}}.7$, $-12^{\circ}17'34''.0$) and the white rectangle near the center shows the area where the IRC NIR spectrum (Figure 7) is extracted. The black rectangles indicate the areas where the fluxes are extracted for the plume-like structures plume 1 ($40'' \times 15''$) and plume 2 ($27'' \times 12''$, see §4.2). The yellow circle of $8''$ in radius shows the region where the flux at the center of the galaxy is estimated. Note that the center of the yellow circle is at the center of the intensity distribution, which is slightly shifted from the center of the galaxy indicated by the white cross (see text).

to around 40%.

Figure 9 shows the SEDs of the three regions in NGC 2782. As a reference SED we also plot the results of sim-

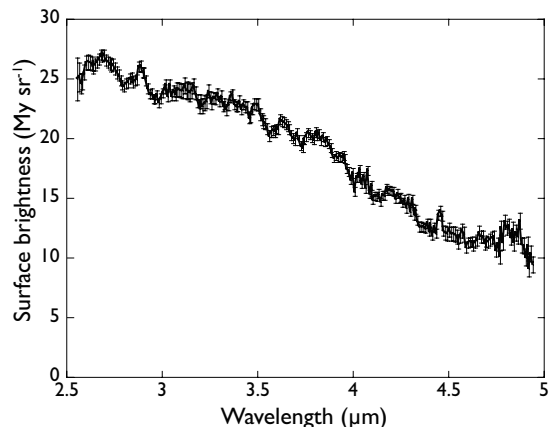


Figure 7. NIR spectrum of the center region of NGC 7727. The region where the spectrum was extracted is indicated by the white rectangle in Figure 6.

ple calculations of the DUSTEM model¹ (Compiègne et al. 2011). All the models are scaled to the observations at $11 \mu\text{m}$. In the DUSTEM calculation, we assume the standard parameters for the model of the diffuse ISM of our Galaxy. We employ the dust properties, size distributions, and ionization fraction of PAHs described in Compiègne et al. (2011) and assume that the mass fraction of PAHs (size between 0.35 and 1.2 nm) as 8.6% , and that of very small grains (VSGs, size between 0.6 and 20 nm) as 1.8% , and that of large grains (LGs, size

¹ <https://www.ias.u-psud.fr/DUSTEM/>

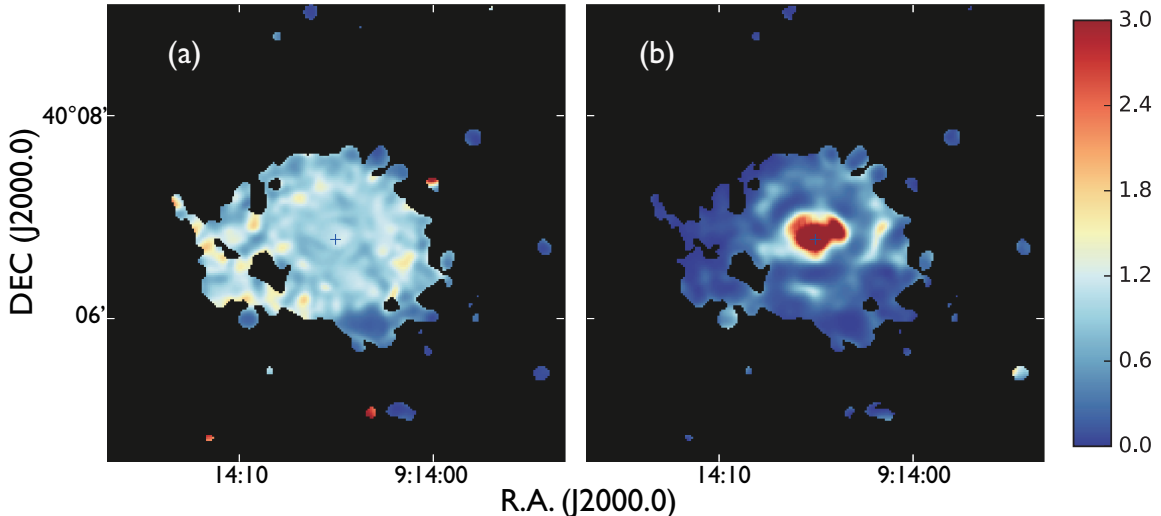


Figure 8. Band ratio maps of NGC 2782. (a) S7 to S11 and (b) L24 to S11 ratios. The pixels with fluxes less than 4σ are masked and shown in black.

between 4 nm and $2\ \mu\text{m}$) as 89.6%. We also assume that the incident radiation field strength U in units of the solar neighborhood is unity. The SED hardly changes as far as U is less than 10 in this spectral range. We assume that the flux at N3 is a summation of the dust emission estimated from model calculations and the contribution from stellar components described above. In Figure 9a, the IRC and IRS spectra of the central region (Figure 4) are also plotted by the thin purple lines. For the IRS spectra, the compact and extended components are added together (§ 2). Since the regions where the spectra are extracted are not exactly the same as the photometric points, each spectrum is scaled to the photometric data points. There are some differences, but the model spectrum is generally in agreement with the observed spectrum at wavelengths below $13\ \mu\text{m}$, where the spectrum of models with $U < 10^3$ does not change appreciably. Excess emission in the NIR relative to the model is also indicated by the IRC spectrum (see below). In Figures 9b and c, we also plot the results of the model spectrum without VSGs to show the VSG contribution. There is no contribution from LGs at wavelengths shorter than $30\ \mu\text{m}$ for $U < 10$ (Li & Draine 2001).

The model flux is slightly larger than the observations at $7\ \mu\text{m}$, in particular, in the tail region. It may be attributed to a decrease of the ionization degree of PAHs since the emission at 6.2 and $7.7\ \mu\text{m}$ is dominated by ionized PAHs, while the emission at $11.3\ \mu\text{m}$ comes mostly from neutral PAHs (Draine & Li 2001; Tielens 2008). A low ratio of the PAH 6.2 and $7.7\ \mu\text{m}$ to $11.3\ \mu\text{m}$ bands are suggested in halos of galaxies (Irwin & Madden 2006; Galliano et al. 2008b), a structure associated with an $\text{H}\alpha$ filament in the dwarf galaxy NGC1569 (Onaka et al. 2010a), and the interarm region of NGC 6946 (Sakon

et al. 2007). The low band ratios seen in these tenuous regions may have a common origin or arise from processing of PAHs in these environments. The low band ratio in the tail region of NGC 2782 is suggested from the medium-band photometry. Spectroscopy of the tail region is certainly needed to confirm the variation in the band ratio quantitatively.

Figure 9 indicates that the SED of the center region increases toward longer wavelengths, while in the ripple and tail regions the SEDs start falling at $15\ \mu\text{m}$. The standard diffuse ISM dust model over-predicts the flux at $24\ \mu\text{m}$ of the ripple region, where the model without VSGs better fits the observed SED. Comparison with the dust model again supports that the star-formation activity is not enhanced in the ripple region.

The SED of the tail falls faster than the ripple region at longer wavelengths and even the model without VSGs cannot explain the observations at 15 and $24\ \mu\text{m}$ well. Since LGs do not contribute to the emission at $24\ \mu\text{m}$ for $U = 1$, it is difficult to explain the observations unless we change the properties of PAHs, which are the dominant contributor in this spectral region next to VSGs. Since larger PAHs contribute to emission at longer wavelengths (Draine & Li 2007), we investigate the effect of the size distribution of PAHs in Appendix A. A simple investigation suggests that even extreme models with only very small PAHs (0.35–0.5 nm) cannot fully explain the observed SEDs. The discrepancy at $24\ \mu\text{m}$ may be attributed to the model emissivity of PAHs rather than to the size distribution. The emission at 15– $24\ \mu\text{m}$ dominantly arises from stochastically heated VSGs and large PAHs. Although simple model calculations cannot explain the observed SED of the tail region consistently, the sharp decline strongly suggests a deficiency of VSGs, and possibly of large PAHs.

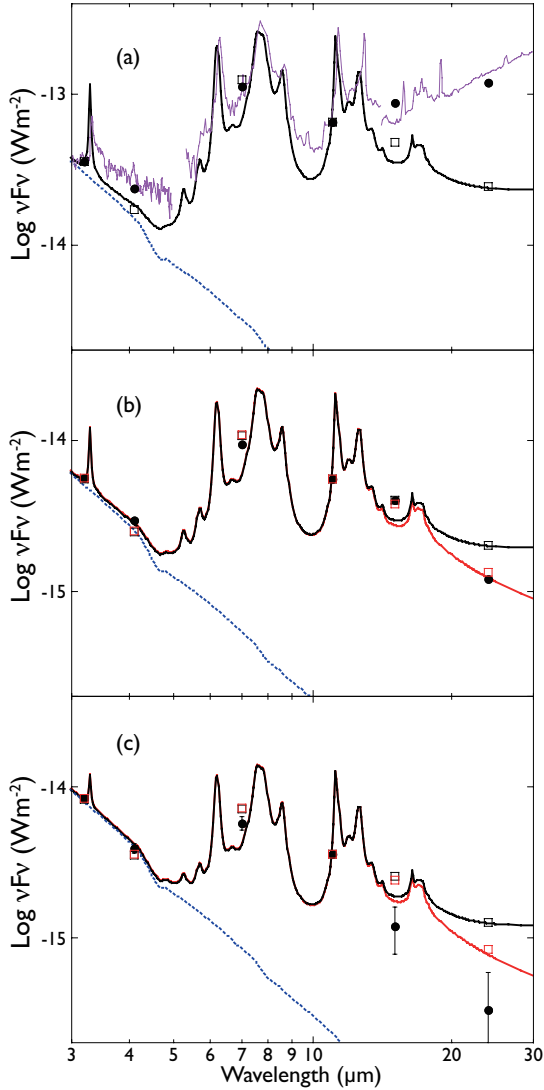


Figure 9. SEDs of three regions of NGC 2782 indicated in Figure 3. (a) Center, (b) ripple, and (c) tail regions. The results of DUSTEM calculations are shown with the black solid lines for $U = 1$ for comparison. They are scaled to the observations at $11 \mu\text{m}$. In (a), the IRC and IRS spectra of the center region (Figure 4) are also plotted by the thin purple lines. The regions where the spectra are extracted are not exactly the same for the photometry and they are scaled at the photometric data. In (b) and (c), the red lines are also plotted to show the DUSTEM results without VSGs (see text). The filled black circles show the IRC photometric results, while the black and red open squares indicate the color-corrected photometric points of the DUSTEM calculations corresponding to the black and red lines, respectively, by taking account of the IRC filter responses (Tanabé et al. 2008). The blue dotted lines indicate the assumed stellar contribution (see text).

In the spectral range $7\text{--}30 \mu\text{m}$, there are several pure rotational transitions of molecular hydrogen (H_2). The L24 band does not have any H_2 lines in its spectral range (both S(0) $28.2 \mu\text{m}$ and S(1) $17.0 \mu\text{m}$ are out of its spectral range), while L15 includes S(1) $17.0 \mu\text{m}$, S11 has S(2) $12.3 \mu\text{m}$ and S(3) $9.7 \mu\text{m}$, and S7 covers

S(4) $8.0 \mu\text{m}$, S(5) $6.9 \mu\text{m}$, and S(6) $6.1 \mu\text{m}$ lines. Therefore, there is a possibility that the H_2 line emissions could make the observed steep decline at $24 \mu\text{m}$ if they make significant contributions to these bands. Roussel et al. (2007) studied the H_2 0–0 S(0)–S(7) transitions in 57 normal galaxies of the *Spitzer* Infrared Nearby Galaxies Survey (SINGS, Kennicutt et al. 2003). They show that the observed fluxes of the S(0)–S(3) transitions are in a range $(1\text{--}400) \times 10^{-18} \text{Wm}^{-2}$. They detect the S(4) to S(7) transitions only in three galaxies in a range $(100\text{--}250) \times 10^{-18} \text{Wm}^{-2}$ with upper limits of about $20 \times 10^{-18} \text{Wm}^{-2}$. They observe either nuclear regions or bright star-forming complexes of the sample galaxies and the observed H_2 emissions originate mostly from PDRs. Larger fluxes ($> 50 \times 10^{-18} \text{Wm}^{-2}$) are seen toward the galaxies, where star-formation activities are large. Their observed areas are typically $\sim 300 \text{arcsec}^2$, which are about an order of magnitude smaller than the area of the tail region (4200arcsec^2) to derive the flux for NGC 2782. The tail region does not have a high star-forming activity (see below). Thus, we estimate that the expected fluxes of S(0)–S(3) transitions in the tail region are at an order of 10^{-16}Wm^{-2} at most, even if we take account of the difference in the size of the observed areas. They are an order of magnitude smaller than the observed fluxes of the tail region at S7, S11, and L15 (Figure 9c). Roussel et al. (2007) indicate that the ratio of the summation of the S(0) to S(2) fluxes to the IRAC band 4 ($8 \mu\text{m}$) flux is relatively constant at around 10^{-2} , which supports the present rough estimate. Although we cannot completely rule out the possibility without spectroscopy, it does not seem to be very likely that the contribution from the H_2 emission is significant in the tail region.

In the center region, the model with $U = 1$ underpredicts the flux at $4.1 \mu\text{m}$, which can be attributed to an uncounted component. Lu et al. (2003) report excess emission in the NIR in normal galaxies, while similar excess is also seen in the diffuse Galactic emission (Flagey et al. 2006). Smith & Hancock (2009) discuss the origin of excess emission at $4.5 \mu\text{m}$ in dwarf galaxies. Onaka et al. (2010a) investigate excess emission in the NIR of the dwarf galaxy NGC 1569, suggesting that the free-free emission estimated from $\text{Br}\alpha$ emission is insufficient to explain the observed emission and favoring the contribution from hot dust. Although it probes only a part of the center region of NGC 2782, we also estimate the contribution from the free-free emission using the observed intensity of $\text{Br}\alpha$ in the IRC NIR spectrum (Figure 4a). The intensity of $\text{Br}\alpha$ is estimated about $4.5 \times 10^{-9} \text{W m}^{-2} \text{sr}^{-1}$, which suggests the free-free emission being less than 0.05MJy sr^{-1} . Therefore, the observed NIR continuum cannot be attributed to the free-free emission and a contribution from the hot

dust component is suggested also for the center region of NGC 2782.

The SED of the center region shows excess emission over the model of $U = 1$ at 15 and 24 μm , suggesting the presence of warm dust. To study the warm dust in the center region quantitatively, we employ data at longer wavelengths. We retrieved the Post-Basic Calibrated Data of NGC 2782 obtained with *Spitzer*/MIPS at 70 and 160 μm (AORKEY: 4348416) from the Spitzer Heritage Archive. Since the MIPS 160 μm data do not have the spatial resolution to resolve the structures of the galaxy, we simply made aperture photometry with a radius of 23.''8 for all the IRC bands as well as MIPS 70 and 160 μm bands to match the PSF of the MIPS 160 μm . The sky background is estimated from the median of the emission outside of the galaxy and subtracted from the data. The total integration time of the MIPS observations at 70 and 160 μm is short, about 120 s and 42 s, respectively, and extended emission is difficult to be detected. The present aperture photometry is made to derive a rough estimate of the SED of the central 23.''8 region of NGC 2782 from NIR to FIR.

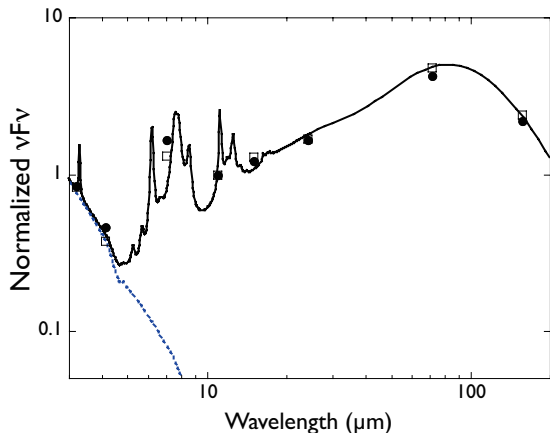


Figure 10. SED of the central region of 23.''8 in radius (filled circles) from the IRC and MIPS observations. The solid line indicates the result of the DUSTEM calculation (see text for details). It is scaled to the observation at 11 μm . The open squares indicate the photometric points of the model spectrum taking account of the color corrections of the filter responses. The blue dotted line indicates the assumed stellar component.

Figure 10 shows the SED of the center region of the IRC and MIPS observations. The SED of the IRC bands is almost identical to that shown in Figure 9a. To compare with the DUSTEM model, we introduce a distribution of U and tune the relative abundances of PAHs, VSGs, and LGs to fit the observation (Figure 10). The model fits the observations fairly well if we assume that the distribution of U is given by a power-law (Dale et al. 2001) with the index of -0.017 , the minimum and maximum U of 7.6 and 10^6 , respectively, and the mass

fractions of PAHs, VSGs, and LGs are 2.8%, 8.2%, and 89%, respectively. The spatial distribution of the infrared emission in galaxies varies with the wavelength and the available FIR data do not have a spatial resolution to resolve small structures. Therefore, the derived parameters of the power-law index and the maximum U should be regarded as rough estimates. The derived parameters support an enhanced star-formation activity in the center region. The derived PAH abundance is small relative to the standard value (8.6%), but is still within a range of normal galaxies (Draine et al. 2007). The small PAH abundance might be related to the destruction of PAHs due to the presence of an AGN. As described above, however, the present IR spectra do not show clear evidence of an AGN. Only recent X-ray observations indicate the presence of a low-luminosity AGN (Tzanavaris & Georgantopoulos 2007; Bravo-Guerrero & Stevens 2017).

Knierman et al. (2013) detected a number of star cluster candidates (SCCs) both in the western and eastern tails. In the western tail, one $\text{H}\alpha$ source is found, but no CO and [C II] 158 μm line emission has been detected. They attribute the absence of the CO and [C II] emission to a low carbon abundance in the western tail. No detection of the MIR emission in the western tail is compatible with their interpretation.

In the eastern tail, several $\text{H}\alpha$ sources are detected as well as the CO and [C II] emission. Knierman et al. (2013) made estimates of SFRs of the regions enclosed by the blue dashed rectangles in Figure 3 from the intensities of $\text{H}\alpha$ and [C II]. Here we use the PAH emission to estimate SFRs of these regions. We measure the fluxes in the S7 band for each region (TDGC, HI-N, HI-M, and HI-S, see Figure 3) and subtract the assumed stellar contribution. The stellar contribution is at most 6% and thus does not affect the conclusion. We assume that the emission at S7 mainly comes from the PAH 6.2 μm and 7.7 μm bands and apply the PAH band-SFR relations provided by Shipley et al. (2016) to estimate the SFR, assuming that the distance is 39.5 Mpc (Knierman et al. 2013). The S7 band collects almost the entire PAH 6.2 and 7.7 μm band fluxes, but it could also have a contribution from other components. Thus, the SFR from the S7 band should be taken as an upper limit. Also note that the spatial resolution of the present observation is different from those of Knierman et al. (2013) and the regions where the estimate made are not exactly the same.

Figure 11 shows comparison of the SFRs thus estimated from the flux at S7 with those from $\text{H}\alpha$ and [C II] for each region. It indicates that the SFR from the PAH bands (S7) is close to that from $\text{H}\alpha$ (TDGC and HI-N) or in between those from $\text{H}\alpha$ and [C II] (HI-M and HI-S). A good correlation between the PAH emission and

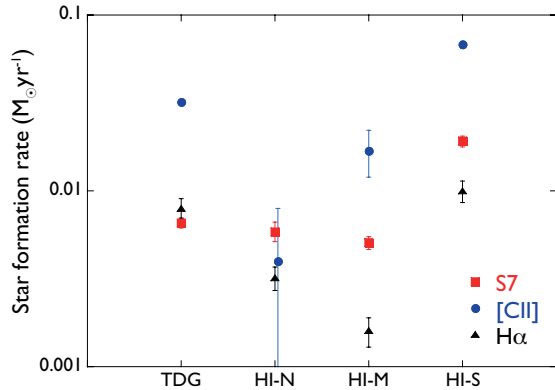


Figure 11. Star-formation rates for the regions indicated in Figure 3. The red squares show those estimated from the PAH bands of the present S7 image (see text for details), while the black triangles and the blue circles indicate those from H α and [C II], respectively (Knierman et al. 2013).

[C II] has been reported for star-forming galaxies, which can be interpreted if the PAHs are the dominant agency for gas heating (Helou et al. 2001). The H α emission indicates the strength of the heating radiation. Taking account of the uncertainties described above, the agreement is sufficiently good. The present results suggest that the PAH emission may be used as a useful measure also for the SFR in these extended structures, although a change in the dust size distribution is suggested. However, the present sample size is too small to draw a general conclusion. We definitely need much more samples to confirm its applicability. To investigate the size distribution and its effect on the estimate of the SFR quantitatively, we need FIR data with a sufficient spatial resolution and sensitivity that allow us to resolve and detect emission from extended structures in the FIR.

4.2. NGC 7727

Figure 12 shows S7 to S11 and L24 to S11 color maps of NGC 7727. The S7 to S11 color is almost constant over the entire galaxy. The L24 to S11 color does not change over the galaxy except for a slight increase in a very small region around the center. The plume regions in the north may suggest a small increase in the band ratio. Compared to the color maps of NGC 2782 (Figure 8), the L24 to S11 band ratio of NGC 7727 is small, suggesting low star-forming activity in NGC 7727.

Figure 13 shows the SEDs of the three regions indicated by the circle and the solid rectangles in Figure 6. The same spectra of the DUSTEM model as in Figure 9 are also plotted with the assumed stellar contribution. Compared to NGC 2782, the contribution from the stellar continuum is estimated to be large. The data at N4 (4.1 μ m) are well explained by the model, suggesting that the assumed spectrum well approximates the stellar

contribution. The NIR spectrum of the center shows a steeply decreasing continuum toward longer wavelengths (Figure 7). This is in agreement with the dominance of the stellar contribution. The DUSTEM model predicts weak PAH emission at 3.3 μ m (Figure 13a), which is not seen in the spectrum. This may suggest the absence of small PAHs that predominantly emit the 3.3 μ m band.

The contribution from the H $_2$ emission can be estimated in a manner similar to §4.1. Since the sizes of the areas from which the fluxes are estimated in the plume regions of NGC 7727 are about the same (600 and 324 arcsec 2 , for plume 1 and plume 2, respectively) as those in the observations of the SINGS galaxy sample (Roussel et al. 2007), we expect that the contribution from the H $_2$ emission is about an order of magnitude smaller (an order of 10^{-17} Wm $^{-2}$) than the observed fluxes (Figures 13b and c) unless the plume regions have high star-formation activities. Spectroscopic studies are certainly needed for the confirmation.

There are clear discrepancies in the flux at 7 μ m for all the three regions, which are larger than that in the tail region of NGC 2782. The model (indicated by open squares) over-predicts the flux at 7 μ m relative to that at 11 μ m. Since the observed S7 to S11 ratio seems to be almost the same as NGC 2782 (Figures 8a and 12a), the difference should be attributed to the larger contribution of the stellar component in NGC 7727. The stellar spectrum has a steep spectral dependence and thus the ISM contribution of NGC 7727 becomes flatter at 7–11 μ m compared to NGC 2782. The resultant ISM SED cannot be explained by the standard PAH emission spectrum. The relatively constant S7 to S11 color suggests that this characteristic of the SED may hold for the entire galaxy.

In addition to low band ratios seen in halo regions, a filament, and an interarm region, elliptical galaxies show peculiar MIR spectra that have the clear PAH 11.3 μ m emission with very weak or almost no emission at 6.2, 7.7, and 8.6 μ m, which are the strongest bands in normal PAH emission spectra (Kaneda et al. 2005, 2007). The IRC NIR spectroscopy also shows that the 3.3 μ m is absent in the elliptical galaxy NGC1316 (Kaneda et al. 2007). These characteristics may be interpreted in terms of emission from large and neutral PAHs. These characteristics seem to accord with the observed MIR SEDs of NGC 7727. In NGC 7727, large and neutral PAHs may dominate due to the weak star-formation activity. NGC 7727 is classified as SAB(s)a pec (de Vaucouleurs et al. 1991), and it may be in a stage to an elliptical galaxy after merging. We certainly need spectroscopy to confirm this interpretation.

The emission of the center region at 11–24 μ m can be explained by the DUSTEM model with $U = 1$, while the SED of the plume regions declines very sharply at

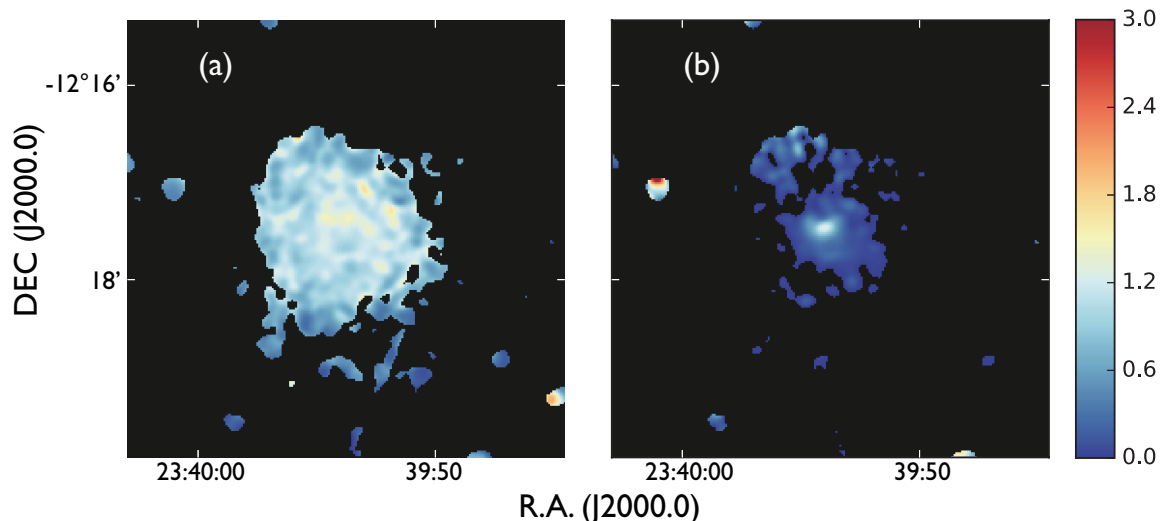


Figure 12. Band ratio maps of NGC 7727. (a) S7 to S11 and (b) L24 to S11. The pixels with fluxes less than 4σ are masked and shown in black.

$24\mu\text{m}$ compared to the DUSTEM model. The fluxes at $24\mu\text{m}$ for the both plumes are less than 3σ and upper limits are plotted in Figures 13b and c. If the fluxes are at the levels that the models predict, they should be detectable and thus the sharp decline at $24\mu\text{m}$ is secure. This is a similar trend seen in the tail region of NGC 2782. Figures 13b and c suggest that even models without VSGs cannot explain the observed SED at $24\mu\text{m}$. We discuss the effects of the size distribution of PAHs in Appendix A similarly to NGC 2782. It seems difficult to explain the observed SEDs solely by the change of the size distribution and the revision of the PAH emissivity at $15\text{--}24\mu\text{m}$ may be needed. Although it may not be typical PAH emission, excess emission at $7\text{--}15\mu\text{m}$ is certainly present (Figure 13). The sharp decline at $24\mu\text{m}$ relative to the excess suggests that the dust that emits predominantly at $24\mu\text{m}$ is deficient in the plume regions of NGC 7727.

4.3. Formation and destruction of PAHs and VSGs

In both galaxies, excess emission at $7\text{--}15\mu\text{m}$ and a sharp decline of the emission at $24\mu\text{m}$ are seen in the extended structures. The sharp decline in the extended structures relative to the Milky Way and the center regions of the galaxy is secure based on the present observations, though the contribution from line emission needs to be investigated by spectroscopy. If the observed SEDs originate mostly from the dust emission that the DUSTEM model simulates, then the decline must be interpreted in terms of the variation in the dust size distribution. The absolute abundance of VSGs depends on the assumed emissivity, but comparison with the DUSTEM model indicates that these regions have a small abundance of VSGs relative to the diffuse ISM of our Galaxy and the center regions of the

galaxy. Since those extended structures are thought to have been formed in the merger events, the deficiency of VSGs must be related to the events. The excess emission at $7\text{--}15\mu\text{m}$ is attributed to the PAH features. In general VSGs are assumed to consist of amorphous carbonaceous dust (Compiègne et al. 2011). The presence of PAHs and the deficiency of VSGs suggest a possible scenario that VSGs fragmented into PAHs in the structures formed during the merger events. The formation of PAHs from fragmentation of carbonaceous dust has been discussed theoretically (Jones et al. 2013; Seok et al. 2014) and suggested in various celestial objects observationally (Onaka et al. 2010a; Seok et al. 2012; Lau et al. 2016). Pilleri et al. (2012, 2014) also study the photo-fragmentation of VSGs into PAHs in PDRs. FIR data with a sufficient spatial resolution and sensitivity are needed to obtain a clear answer if the fraction of PAHs increases relative to LGs by fragmentation and/or if the entire dust size distribution is changed (§4.1).

If the observed SEDs are the results of fragmentation of VSGs into PAHs during the merger events, the size distribution of PAHs and VSGs must have been preserved since then. The proposed scenario requires that the destruction time scale of PAHs and the formation time scale of VSGs should be longer than the merger ages. The merger age is estimated as about 200–300 Myr for NGC 2782 (Smith 1994; Knierman et al. 2013) and 1.3 Gyr for NGC 7727 (Georgakakis et al. 2000). In our Galaxy, the lifetime of carbonaceous dust is estimated as 170 Myr (Serra Díaz-Cano & Jones 2008) and that of PAHs is as $\sim 100\text{--}500$ Myr (Micelotta et al. 2010). Recently Bocchio et al. (2014) re-evaluate that the lifetime of carbonaceous dust is even shorter as $\approx 62 \pm 56$ Myr by merging the inertial and thermal sputtering into a single process. We try a very rough estimate to translate the

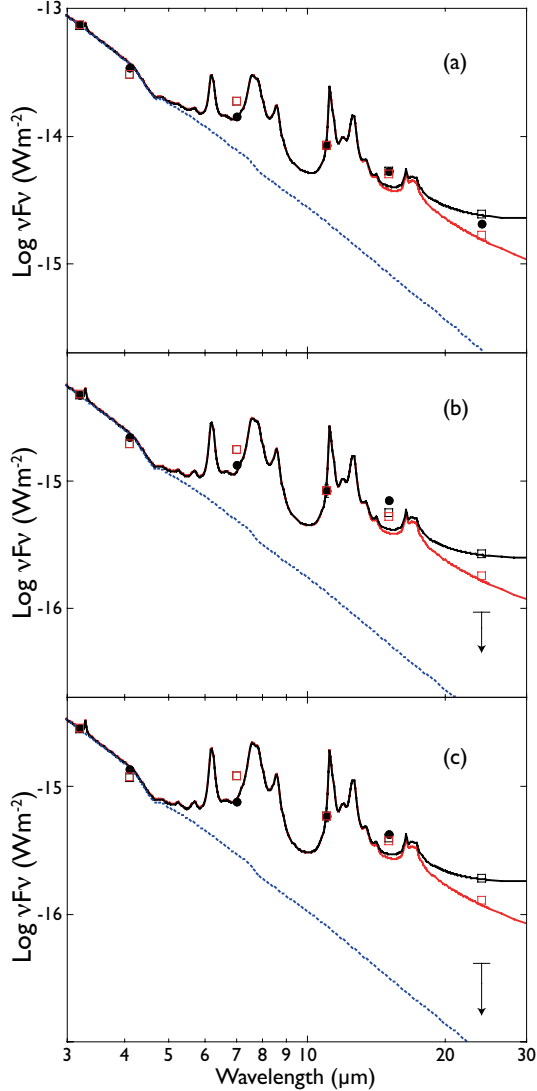


Figure 13. SEDs of three regions of NGC 7727 indicated in Figure 6. (a) Center, (b) plume 1, and (c) plume 2 regions. The results of DUSTEM calculations are shown by the black and red lines for $U = 1$ for the models with and without VSGs, respectively. They are scaled to the observations at $11 \mu\text{m}$. The filled black circles show the IRC photometric results, while the black and red open squares indicate the color-corrected photometric points of the DUSTEM calculations corresponding to the black and red lines, respectively. The blue dotted lines indicate the assumed stellar contribution.

lifetime in our Galaxy to the tail region in NGC 2782 and the plume regions in NGC 7727. Supernova shocks are the dominant destruction process and thus the lifetime must be related to the SFR. The estimated total SFRs in the tail region of NGC 2782 is $0.02\text{--}0.13 M_{\odot}\text{yr}^{-1}$ (Figure 11, Knierman et al. 2013). Chomiuk & Povich (2011) collect various estimates of the SFR of our Galaxy and derive an average value of $1.9 \pm 0.4 M_{\odot}\text{yr}^{-1}$, while Licquia & Newman (2015) apply a hierarchical Bayesian statistical method and obtain $1.65 \pm 0.19 M_{\odot}\text{yr}^{-1}$. The area of the tail region indicated in Figure 3 is about

150 kpc^2 at a distance of 39.5 Mpc, which is about half a size of the surface area of our Galaxy disk. If it is inversely proportional to an average SFR per area, the destruction time scale in the tail region can be by an order of magnitude longer than the Galactic value. Thus, it may be longer than the merger age. We do not have much information on the SFR in the plume regions of NGC 7727. Although their PAH features do not seem to be typical and thus it has a large uncertainty, we use the S7 band flux to infer their SFRs. The observed fluxes at S7 in the plume regions are smaller by about an order of magnitude than that of the tail region of NGC 2782 (Figures 9c, 13b, and c), suggesting that the SFR per area is also smaller. The lifetime of PAHs in these regions may be two orders of magnitude longer than the Galactic value and thus may be longer than its merger age.

The estimated very short destruction time scale of carbonaceous dust in our Galaxy suggests rapid recycling of carbonaceous dust in our Galaxy. To compensate the rapid destruction, it is generally suggested that dust grows in dense clouds in a similar timescale (e.g., Jones & Nuth 2011; Bocchio et al. 2014). Direct conversion of these values into the formation time scales of carbonaceous dust in the tail and plume regions is not straightforward, but these investigations suggest that formation of carbonaceous dust, thus VSGs, requires dense clouds and must also be related to the star-formation activity. The suggested low SNRs per area in the extended regions of both galaxies indicate a longer time scale also for the formation of carbonaceous dust, including VSGs. Although these estimates are very rough, the destruction of PAHs and the formation of VSGs may take a longer time than the merger ages due to the low star-formation activities for both galaxies. Then, the size distribution of PAHs and VSGs may have been preserved after the merger events until now.

It should be noted that the above discussion is made on the basis of medium-band photometry. While emission of molecular hydrogen should not contribute to the present results significantly as discussed above, contributions from other lines or features cannot be ruled out completely. Spectroscopic study is definitely needed to support the above discussion and interpretation.

5. SUMMARY

We present NIR to MIR imaging and NIR spectroscopic observations of the two mergers, NGC 2782 and NGC 7727, with *AKARI*/IRC. The MIR to FIR SED suggests enhanced star-formation activities in the central part of NGC 2782. No evidence for the presence of an AGN is obtained in the present observations. The ripples seen in optical images of NGC 2782, which are thought to have been formed by the merger event, are

also seen in the MIR images. The SED suggests no enhancement in the star-formation in the ripples. The IR SED of NGC 7727 is dominated by the stellar component. Neither PAH $3.3\ \mu\text{m}$ emission nor H I recombination lines are detected in the central part of the galaxy, suggesting a low star-formation activity.

NGC 2782 shows extended emission (tail structure) at $7\text{--}15\ \mu\text{m}$, whose structure well corresponds to the eastern tidal tail seen in the H I map. NGC 7727 shows extended emission (plumes) at $7\text{--}15\ \mu\text{m}$, similar structure to which has been seen in the K -band image. Both structures are thought to have been formed by the merger events. The SED of the tail of NGC 2782 at $7\text{--}15\ \mu\text{m}$ can well be explained by PAH emission with a smaller ionization degree of PAHs relative to the diffuse ISM of our Galaxy. The SEDs of the plume regions of NGC 7727 suggest PAH emission of much lower ionization degree. It may be similar to those seen in elliptical galaxies. Spectroscopic studies are definitely needed to confirm the nature of their emission.

Extended emissions in both galaxies decline more rapidly at $24\ \mu\text{m}$ than the model SED of the ISM of our Galaxy, suggesting a deficiency of VSGs. While it must be confirmed by spectroscopy that emission lines or other features do not contribute to the observed fluxes significantly, the observed SEDs of the extended emission can be interpreted if VSGs fragment into PAHs during the merger events. Because of the low star-formation activities in both regions, the time scales for the destruction of PAHs and formation of VSGs may be longer than the merger ages. Then, the present infrared SEDs retain the imprint of the size distribution of PAHs and VSGs created during the merger events.

The star-formation rate of the tail region of NGC 2782 estimated from the $7\ \mu\text{m}$ band is in agreement with those

estimated from H α and [C II] $158\ \mu\text{m}$. The present results suggest that the PAH emission may also be used as a star-formation rate measure for extended structures of galaxies despite possible processing of dust grains in these regions. However, the number of the present sample is too small to draw a general conclusion. We certainly need much larger samples to test its applicability. The present results also suggest that MIR observations are very efficient to identify and study extended structures formed by merger events and to study processing of dust in merger events. Further studies with FIR data that allow us to quantitatively investigate the size distribution of dust in structures associated with merger events will provide a unique opportunity to investigate the dust lifetime and processing in a galactic time scale and its effect on the estimate of the SFR from the PAH emission.

This work is based on observations with *AKARI*, a JAXA project with the participation of ESA. The authors thank all the members of the *AKARI* project for their continuous support. This research has made use of the NASA/IPAC Infrared Science Archive and the NASA/IPAC Extragalactic Database (NED), both of which are operated by the Jet Propulsion Laboratory, California Institute of Technology, under contract with the National Aeronautics and Space Administration. R. W. was supported by the Japan Society for the Promotion of Science (JSPS) as an International Research Fellow. This work is supported by JSPS and CNRS under the Japan – France Research Cooperative Program and a grant for Scientific Research from the Japan Society for the Promotion of Science (nos. 23244021).

Facilities: AKARI, Spitzer

APPENDIX

A. MODEL CALCULATIONS OF MODIFIED SIZE DISTRIBUTION OF PAH

To explain the sharp decline seen at $15\text{--}24\ \mu\text{m}$ in the SEDs of the tail region of NGC 2782 and the plume regions of NGC 7727, we investigate the effects of the PAH size distribution by a simple model analysis. The size distribution of PAHs in the original model is given by a log-normal distribution between $0.35\ \text{nm}$ and $1.2\ \text{nm}$. Larger PAHs contribute to emission at longer wavelengths (Draine & Li 2007). We decrease the maximum size and compare the model with the observations in Figure A1 (black lines). The spectra are normalized at $11\ \mu\text{m}$ for comparison. We found that the observed flux at $24\ \mu\text{m}$ relative to that at $11\ \mu\text{m}$ can be explained if we assume the presence of only small PAHs of $0.35\text{--}0.5\ \text{nm}$. The assumed size distribution is very extreme and contrived, and is used only for investigation of the size effect. However, even the model that has such an extreme size distribution cannot be reconciled with the observed flux at $15\ \mu\text{m}$ satisfactorily. In addition, because of the size distribution biased toward smaller PAHs, the model flux at $7\ \mu\text{m}$ exceeds well above the observation.

The 6.2 and $7.7\ \mu\text{m}$ PAH bands are enhanced when PAHs are ionized (Draine & Li 2001; Tielens 2008). In the standard model, the size-dependent ionization fraction of PAHs is assumed and the ionization fraction of small PAHs is around 38% (Compiègne et al. 2011). To investigate the effect of the ionization fraction in addition to the size distribution, we also calculate the model with the same size distribution of only small PAHs, assuming that they are all neutral. The resultant model spectrum is shown by the red lines in Figure A1. Small neutral PAH model may

explain the observations at 7, 11, and 24 μm , but the discrepancy at 15 μm is increased. It should also be noted that the models with only small PAHs predict very strong PAH emission at 3.3 μm , which should be detectable in the N3 image. Taking account of these facts, simple modifications of the size distribution and the ionization degree of PAHs have difficulties in explaining the observed SEDs consistently, suggesting that the modification of the PAH emissivity may be needed to fully explain the observed SEDs of the tail of NGC 2782 and the plume regions of NGC 7727.

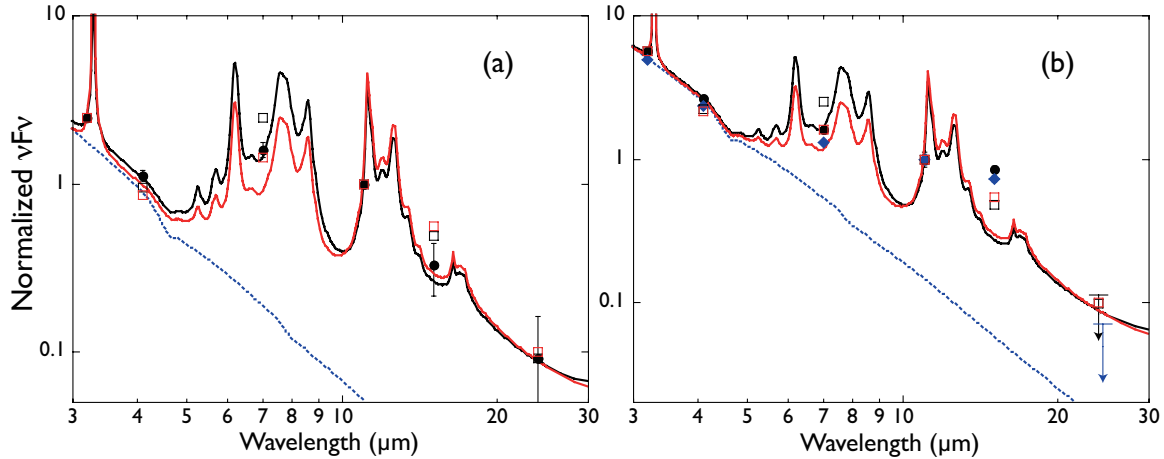


Figure A1. Normalized SEDs of (a) the tail region of NGC 2782 (filled circles) and (b) the plume regions of NGC 7727 (the filled black circles for plume 1 and the filled blue diamonds for plume 2). The black and red lines show the DUSTEM model with only small PAHs and that with small, neutral PAHs, respectively (see text). The black and red open squares indicate the photometric points of the model spectra of the black and red lines, respectively, taking account of the color corrections of the filter responses. The blue dotted lines indicate the assumed stellar component. The spectra are normalized at 11 μm for comparison.

REFERENCES

- Armus, L., Charmandaris, V., Bernard-Salas, J., et al. 2007, *ApJ*, 656, 148
- Baba, S., Nakagawa, T., Shirahata, M., et al. 2016, *PASJ*, 68, 27
- Beirão, P., Brandl, B. R., Appleton, P. N., et al. 2008, *ApJ*, 676, 304
- Bocchio, M., Jones, A. P., & Slavin, J. D. 2014, *A&A*, 570, A2
- Boer, B., Schulz, H., & Keel, W. C. 1992, *A&A*, 260, 67
- Braine, J., Duc, P.-A., Lisenfeld, U., et al. 2001, *A&A*, 378, 51
- Brassington, N. J., Zezas, A., Ashby, M. L. N., et al. 2015, *ApJS*, 218, 6
- Bravo-Guerrero, J., & Stevens, I. R. 2017, *MNRAS*, 467, 3788
- Carey, S. J., Lacy, M. D., Seppo, J. L., et al. 2006, *Proc. SPIE*, 5487, 211
- Chomiuk, L., & Povich, M. S. 2011, *AJ*, 142, 197
- Compiègne, M., Verstraete, L., Jones, A., et al. 2011, *A&A*, 525, A103
- Dale, D. A., Helou, G., Contursi, A., Silbermann, N. A., & Kolhatkar, S. 2001, *ApJ*, 549, 215
- de Vaucoullers, G., de Vaucoullers, A., Corwin, H. G., Jr., Buta, R. J., Paturel, G., & Fouque, P. 1991, *Third Reference Catalogue of Bright Galaxies* (Springer, New York)
- Draine, B. T., & Li, A. 2001, *ApJ*, 551, 807
- Draine, B. T., & Li, A. 2007, *ApJ*, 657, 810
- Draine, B. T., Dale, D. A., Bendo, G., et al., 2007, *ApJ*, 663, 866
- Dwek, E., & Scalo, J. M. 1980, *ApJ*, 239, 193
- Engelbracht, C. W., Kundurthy, P., Gordon, K. D., et al. 2006, *ApJL*, 642, L12
- Fabian, A. C., Nulsen, P. E. J., & Steward, G. C. 1980, *Nature*, 287, 613
- Farrah, D., Bernard-Salas, J., Lonsdale, Spoon, H. W. W., et al. 2007, *ApJ*, 667, 149
- Flagey, N., Boulanger, F., Verstraete, L., et al. 2006, *A&A*, 453, 969
- Galliano, F., Dwek, E., & Charnial, P. 2008a, *ApJ*, 672, 214
- Galliano, F., Madden, S. C., Tielens, A. G. G. M., Peeters, E., & Jones, A. P. 2008b, *ApJ*, 679, 310
- Georgakakis, A., Forbes, D. A., & Norris, R. P. 2000, *MNRAS*, 318, 124
- Helou, G., Malhotra, S., Hollenbach, D. J., Dale, D. A., & Contursi, A. 2001, *ApJL*, 548, L73
- Herbst, E. 1991, *ApJ*, 366, 133
- Hernquist, L., & Quinn, P. J. 1988, *ApJ*, 331, 682
- Hernquist, L., & Spergel, D. N. 1992, *ApJL*, L117
- Higdon, S. J. U., Devost, D., Higdon, J. L., et al. 2004, *PASP*, 116, 975
- Houck, J. R., Roellig, T. L., van Cleve, J., et al. 2004, *ApJS*, 154, 18
- Howard, S., Keel, W. C., Byrd, G., & Burkey, J. 1993, *ApJ*, 417, 502
- Hunt, L. K., Combes, F., García-Burillo, E., et al. 2008, *A&A*, 482, 133
- Irwin, J. A., & Madden, S. C. 2006, *A&A*, 445, 123
- Ishihara, D., Onaka, T., Kaneda, H., et al. 2007, *PASJ*, 59, S443
- Jogee, S., Kenney, J. D. P., & Smith, B. J. 1999, *ApJ*, 526, 665
- Jones, A. P., & Nuth, J. A. 2011, *A&A*, 530, A44
- Jones, A. P., Fanciullo, L., Köhler, M., et al. 2013, *A&A*, 558, A62
- Kaneda, H., Onaka, T., & Sakon, I. 2005, *ApJL*, 632, L83
- Kaneda, H., Onaka, T., & Sakon, I. 2007, *ApJL*, 666, L21

- Kaneda, H., Koo, B. C., Onaka, T., & Takahashi, H. 2009a, *AdSpR*, 44, 1038
- Kaneda, H., Ishihara, D., Suzuki, T., et al. 2010, *A&A*, 514, A14
- Kennicutt, R. C., Jr. 1998, *ARA&A*, 36, 189
- Kennicutt, R. C., Jr., Armus, L., Bendo, G., et al. 2003, *PASP*, 115, 928
- Knierman, K. A., Scowen, P., Veach, T., et al. 2013, *ApJ*, 774, 125
- Kwok, S., & Zhang, Y. 2011, *Nature*, 479, 80
- Lau, R. M., Werner, M., Sahai, R., & Ressler, M. E. 2016, *ApJ*, 833, 115
- Lebouteiller, V., Bernard-Salas, J., Sloan, G. C., & Barry, D. J. 2010, *PASP*, 122, 231
- Lebouteiller, V., Barry, D. J., Spoon, H. W. W., et al. 2011, *ApJS*, 196, 8
- Lebouteiller, V., Barry, D. J., Goes, C., et al. 2015, *ApJS*, 218, 21
- Li, A., & Draine, B. T. 2001, *ApJ*, 554, 778
- Licquia, T. C., & Newman, J. A. 2015, *ApJ*, 806, 96
- Lu, N., Helou, G., Werner, M. W., et al. 2003, *ApJ*, 588, 199
- Lucy, L. B. 1974, *AJ*, 79, 745
- Micelotta, E. R., Jones, A. P., & Tielens, A. G. G. M., 2010a, *A&A*, 510, A36
- Micelotta, E. R., Jones, A. P., & Tielens, A. G. G. M., 2010b, *A&A*, 510, A37
- Mould, J. R., Huchra, J. P., Freedman, W. L., et al. 2000, *ApJ*, 529, 786
- Ohyama, Y., Onaka, T., Matsuhara, H., et al. 2007, *PASJ*, 59, S411
- Onaka, T., Tokura, D., Sakon, I., et al. 2007a, *ApJ*, 654, 844
- Onaka, T., Matsuhara, H., Wada, T., et al. 2007b, *PASJ*, 59, S401
- Onaka, T., Lorente, R., Ita, Y., Ohyama, Y., Tanabé, T., & Pearson, C. 2009, *AKARI IRC Data User Manual for Post-Helium (Phase 3) Mission*, ver1.1, <http://www.ir.isas.jaxa.jp/AKARI/Observation/support/IRC/IDUM/IRC.IDUM.P3.1.1.pdf>
- Onaka, T., Matsumoto, H., Sakon, I., & Kaneda, H. 2010a, *A&A*, 514, A15
- Onaka, T., Matsuhara, H., Wada, T., et al. 2010b, *Proc. SPIE*, 7731, 77310M
- Quinn, P. J. 1984, *ApJ*, 279, 596
- Paradis, D., Reach, W. T., Bernard, J.-P., et al. 2009, *AJ*, 138, 196
- Peeters, E., Spoon, H. W. W., & Tielens, A. G. G. M. 2004, *ApJ*, 613, 986
- Petric, A. O., Armus, L., Howell, J., et al. 2011, *ApJ*, 730, 28
- Pilleri, P., Montillaud, J., Berné, O., & Joblin, C. 2012, *A&A*, 542, A69
- Pilleri, P., Joblin, C., Boulanger, F., & Onaka, T. 2014, *A&A*, 577, A16
- Pope, A., Chary, R.-R., Alexander, D. M., et al. 2008, *ApJ*, 675, 1171
- Richardson, W. H. 1972, *J. Opt. Soc. Am.*, 62, 55
- Roussel, H., Helou, G., Hollenbach, D. J., et al. 2007, *ApJ*, 669, 959
- Rothberg, B., & Joseph, R. D. 2004, *AJ*, 128, 2098
- Sakata, A., Wada, S., Tanabé, T., & Onaka, T. 1984, *ApJL*, 287, L51
- Sakon, I., Onaka, T., Kaneda, H., et al. 2006, *ApJ*, 651, 174
- Sakon, I., Onaka, T., Wada, T., et al. 2007, *PASJ*, 49, S483
- Sandage, A., & Tammann, G. A. 1981, *A Revised Shapley-Ames Catalog of Bright Galaxies* (Carnegie Institution, Washington)
- Sandstrom, K., Bolatto, A., Draine, B. T., Bot, C., & Stanimirović, S. 2010, *ApJ*, 715, 701
- Seok, J. Y., Koo, B.-C., & Onaka, T. 2012, *ApJ*, 744, 160
- Seok, J. Y., Hirashita, H., & Asano, R. S. 2014, *MNRAS*, 439, 2186
- Serra Díaz-Cano, L., & Jones, A. P. 2008, *A&A*, 492, 127
- Shiple, H., Papovich, C., Rieke, G., Brown, M. J. I., & Moustakas, J. 2016, *ApJ*, 818, 60
- Smith, B. 1994, *AJ*, 107, 1695
- Smith, B., Struck, C., Kenney, J. D. P., & Joglee, S. 1999, *AJ*, 117, 1237
- Smith, J. D., Draine, B. T., Dale, D. A., et al. 2007a, *ApJ*, 656, 770
- Smith, B. J., Struck, C., Hancock, M., Appleton, P. N., Charmandaris, V., & Reach, W. T. 2007b, *AJ*, 133
- Smith, B. J., & Hancock, M. 2009, *AJ*, 138, 130
- Starck, J.-L., & Murtagh, F. 1994, *A&A*, 288, 342
- Tanabé, T., Sakon, I., Cohen, M., et al. 2008, *PASJ*, 60, S375
- Thomson, R. C., & Wright, A. E. 1990, *MNRAS*, 247, 122
- Tielens, A. G. G. M. 2008, *ARA&A*, 46, 289
- Tomassini, S., Spinoglio, L., Malkan, M. A., & Fazio, G. 2010, *ApJ*, 709, 1257
- Tzanavaris, P., & Georgantopoulos, I. 2007, *A&A*, 468, 129
- Wallin, J. F., & Struck-Marcell, C. 1988, *AJ*, 96, 1850
- Yoshida, M., Tanuguchi, Y., & Murayama, T. 1994, *PASJ*, 46, L195